Chinese Chemical Letters 32 (2021) 3123–3127

Contents lists available at ScienceDirect

Chinese Chemical Letters

journal homepage: www.elsevier.com/locate/cclet

Communication

Formation mechanism and properties of NiCoFeLDH@ZIF-67 composites

Huijie Zhou[a], Weiyi Cao[a], Nuochen Sun[a], Li Jiang[a], Yong Liu[b], Huan Pang[a,*]

[a] School of Chemistry and Chemical Engineering, Yangzhou University, Yangzhou 225009, China
[b] Collaborative Innovation Center of Nonferrous Metals of Henan Province, Henan Key Laboratory of High Temperature Structural and Functional Materials, School of Materials Science and Engineering, Henan University of Science and Technology, Luoyang 471023 China

ARTICLE INFO

Article history:
Received 18 February 2021
Received in revised form 15 March 2021
Accepted 19 March 2021
Available online 22 March 2021

Keywords:
Formation
Mechanism
NiCoFeLDH@ZIF-67
Composite
Surpercapacitor

ABSTRACT

Metal–organic frameworks (MOFs) have a regular porous structure and high porosity, which make them ideal electrode materials for supercapacitors. However, their capacitance performance is greatly limited by their poor conductivity. In this study, a multi-component hierarchical structure was obtained by growing NiCoFeLDH on the surface of ZIF-67, which increased the electron transfer between the MOF particles and greatly improved the capacitance of ZIF-67. The formation mechanism of the multi-component layered hollow structure indicated that the hydrolysis acidity of metal ions and the coordination ability with ligands were the key factors for forming nanosheets and hollow structures. By controlling the type and valence state of the doped metals and the reaction time, the morphology transformation of MOF composites can be effectively controlled. Electrochemical studies showed that the specific capacitance of hollow NiCoFeLDH@ZIF-67 composite is 1202.08 F/g (0.5 A/g). In addition, aqueous devices were assembled and carefully tested. This scheme is crucial for the design of MOF-based materials used in supercapacitor devices and serves as a guide for the design of MOF-based composites.

Metal–organic frameworks (MOFs) represent a new type of porous materials and have been preferred as electrode materials owing to their ordered porous and adjustable structure as well as large specific surface area [1–8]. The morphology of MOFs can be adjusted by choosing different organic ligands and suitable surfactants [9–15]. In addition, the application of MOFs as templates is an effective novel strategy for the synthesis of various new structures [16–19]. For example, Xia *et al.* [20] obtained supercapacitor electrode materials with excellent electrochemical properties by simple thermal activation of the monodisperse metal oxide hollow nanoparticles (NPS) from large MOF crystals. Qu *et al.* [21] synthesized NiCoMOF-74, which is a metal-functionalized hydroxide with high porosity; this material been used as an electrode material for supercapacitors with good cycle stability and energy density. Liu *et al.* [22] prepared mesoporous nanoporous carbon with a high specific surface area and excellent electrochemical performance using MOF-5 as a template for supercapacitor electrode materials. Qu *et al.* [23] used MOF-based electrode materials to prepare electrode materials for hybrid supercapacitors by employing a "one-for-all" strategy, which has a wide applicability and exhibits an excellent electrochemical performance. Wang *et al.* [24] demonstrated that a conductive MOF/layered double hydroxide (cMOF/LDH) heteronanotube array had excellent oxygen evolution activity based on crystal matching growth.

Zeolites based on an imidazole framework (ZIFs) have uniform pores, a large specific surface area, and good chemical stability and are therefore promising energy storage materials [25–28]. Cobalt-based ZIFs (ZIF-67) have been widely studied as energy storage materials. ZIF-67 alone can be easily agglomerated in a solution, but the solution has a poor conductivity and low stability, resulting in low interfacial reaction kinetics [29,30]. Therefore, the use of ZIF-67 alone as a supercapacitor material is limited. However, as ZIF-67 is a porous material with good crystallinity and easily adjustable crystal structure, it can be constructed into a central control frame structure with adjustable composition and morphology [31–33]. Under controlled conditions, composite electrode materials with ZIF-67 as the template and precursor can be obtained using methods such as ion exchange, calcination, chemical corrosion and precursor conversion [34–42]. Combining ZIF-67 with other electrode materials can synergistically enhance the physical/chemical properties of a single material. In recent years, ZIF-67 has been used as the precursor and coated with a polypyrrole (PPy) layer to obtain hollow materials exhibiting a

* Corresponding author.
E-mail address: panghuan@yzu.edu.cn (H. Pang).

https://doi.org/10.1016/j.cclet.2021.03.050

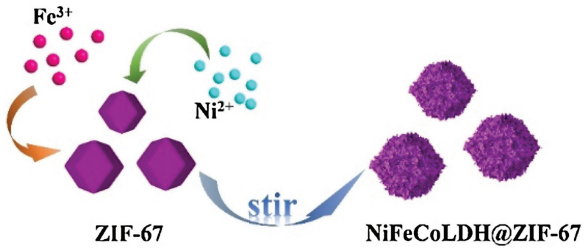

Scheme 1. The synthesis diagram of NiCoFeLDH@ZIF-67.

good electrochemical storage performance [43]. In addition, transition-metal-based layered double hydroxides (LDHs) exhibit a large theoretical capacity and good conductivity, low cost, and rich redox states; thus, they are suitable candidates as supercapacitor electrode materials [44]. The hierarchical structures of the MOFs and LDH composites can effectively contribute to the electrochemical reaction and improve the storage performance of materials [45,46].

In this work, ZIF-67 was used as the precursor to controllably synthesize a hollow-structure NiCoFeLDH@ZIF-67 composite by introducing Ni^{2+} and Fe^{3+}. The unique structure of the composite can increase the contact area required for the electrochemical reaction, which is conducive to the mass transfer of the electrolyte to improve Faraday redox reactions. In addition, the uniform compounding of LDH and ZIF-67 increases the activity and stability of ZIF-67. The specific capacitance of the hollow composite NiCoFeLDH@ZIF-67 was 1202.08 F/g in 3.0 mol/L potassium hydroxide (KOH) solution at 0.5 A/g, which is better than that of ZIF-67. In addition, we separately introduced Ni^{2+}, Fe^{3+} and Fe^{2+} to analyze the effects of different metals and valence ions on the structure and morphology; we also explored the formation mechanism of the hollow structure of the NiCoFeLDH@ZIF-67 composite. To some extent, the formation of the hollow structure can be related to the effect of the pH of the added substances in the solution on the degree of hydrolysis. This study presents a controllable strategy for the synthesis of mesoporous composites and has a certain guiding significance for the synthesis of composites of LDH and other MOF materials.

The synthesis diagram of NiCoFeLDH@ZIF-67 is shown in Scheme 1. The precursor was synthesized by a previously reported synthesis method and used to prepare the composite [45]. As shown in Fig. 1a, ZIF-67, Ni^{2+} and Fe^{3+} were stirred at room temperature for 0.5, 2 and 6 h, respectively, to obtain composite materials with different internal structures (denoted as H1, H2 and H3, respectively). The change in morphology with the stirring time was studied. The structure and morphology of each sample were characterized by transmission electron microscopy (TEM) and scanning electron microscopy (SEM). The morphologies of ZIF-67, H1, H2 and H3 were characterized by SEM. As shown in Figs. $1b_1$–e_1, the surface of ZIF-67 was changed by the doping with Ni^{2+} and Fe^{3+}. With the increase in stirring time, the surface of ZIF-67 gradually transformed into a regular flake. Figs. $1c_2$–e_2 show the TEM diagrams of samples H1, H2 and H3. As can be seen from the TEM characterization, there is no cavity in the polyhedron of sample H1; however, compared with the TEM diagram of the ZIF-67 precursor (Fig. $1b_2$), there is a lamellar structure on the surface. With the increase in the stirring time, the nucleus of ZIF-67 gradually became smaller and a hollow structure was finally formed after 6 h of stirring.

The hollow structure of ZIF-67 was formed only when the stirring time was appropriate. Figs. 2a–c show the TEM diagram of H3. It can be seen that ZIF-67 completely transformed into a hollow structure that retains the ZIF-67 dodecahedron. The outer layer has a sheet structure. The selected area electron diffraction (SAED) and

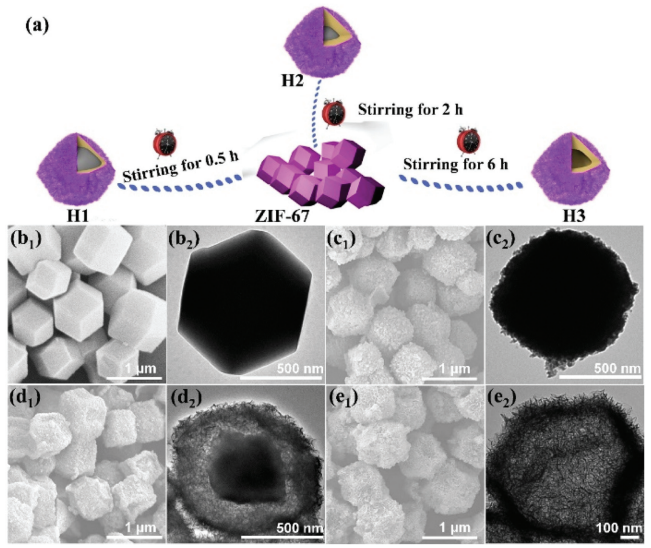

Fig. 1. Structural characterization of all sample. (a) Diagram of formation of H1, H2 and H3. (b1, c1, d1, e1) SEM image of ZIF-67, H1, H2 and H3. (b2, c2, d2, e2) TEM image of ZIF-67, H1, H2 and H3.

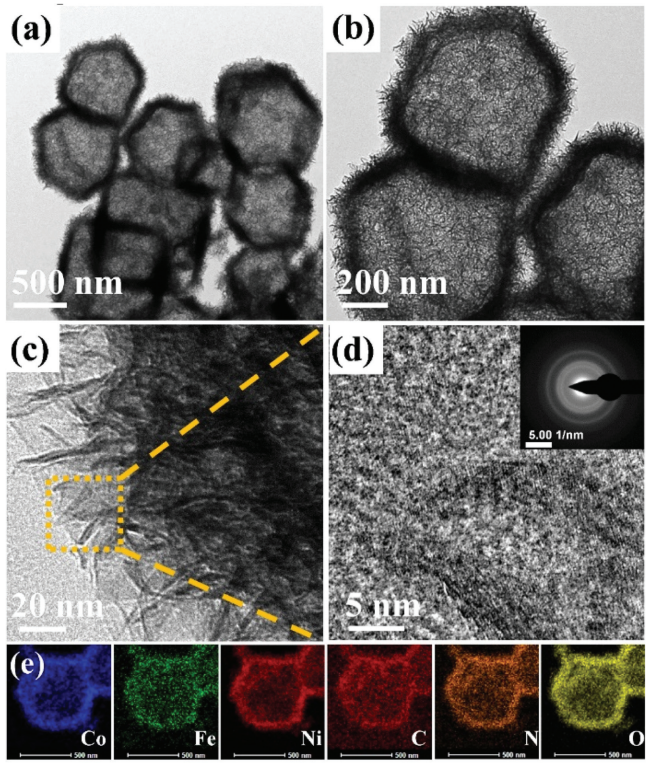

Fig. 2. Structural characterization of H3 particles. (a,b) The low-magnified TEM image. (c) The high-magnified TEM images. (d) The HRTEM image and SAED pattern (inset). (e) the EDX-elemental mapping of Co, Fe, Ni, C, N and O.

high-resolution TEM (HRTEM) patterns show that there are no noticeable diffraction rings and lattice fringes (Fig. 2d). This is because the main component of the material is ZIF-67, which has no noticeable lattice fringes and diffraction rings because the crystal structure is destroyed by the high-energy electron beam excitation. The elemental mapping results (Fig. 2e) show the uniform distribution of Co, Fe, Ni, N, O and C and further explain the successful incorporation of Fe and Ni.

Using ZIF-67 as a framework template, hollow polyhedral nanostructures can be prepared. As can be seen in the XRD diagram, it can be seen from the XRD patterns that the relative intensity and local position of the characteristic diffraction peaks of H1, H2 and H3 (when 2θ is about 7.38°, 10.37°, 12.79°, 14.74°, 16.48°, 18.08° and 22.22°) are well matched with the standard XRD patterns of ZIF-67 (Fig. 3a). However, it can be seen that the crystallinity of H3 changes in a certain extent when the peak position is 22.22°, but the peak position does not change noticeably compared with that of ZIF-67. Fig. 3b shows the Fourier-transform infrared (FT-IR) spectra of various structural samples in the range of 400–4000 cm^{-1}. The stretching and bending modes of the imidazole ring correspond to at the peak position in the range of 600–1500 cm^{-1}. Both 3409 and 3200–3500 cm^{-1} correspond to stretching vibration modes of the hydroxyl group. The vibration modes of 1580–2929 and 3135 cm^{-1} were attributed to C=N, C—H and 2-methylimidazole, respectively. With the introduction of Ni^{2+} and Fe^{3+}, the peak positions of H1, H2 and ZIF-67 did not change significantly, while the peak positions of the hydroxyl group shifted higher. Compared with ZIF-67, H3 had more hydroxyl peaks between 3409 and 3200–3500 cm^{-1}. Although the bond between C=N of the imidazole ring at 1579 and 600–1500 cm^{-1} is partially broken, the basic bond structure remains unchanged.

X-ray photoelectron spectroscopy (XPS) was used to further characterize the surface element composition. As shown in Fig. 3c, there are certain main peaks of Fe 2p, Co 2p, Ni 2p, O 1s, C 1s and N 1s in the full spectrum of samples H1, H2 and H3. In addition, the high-resolution spectrum of Co 2p is shown in Fig. 3d. After adding Ni and Fe, the position of the Co 2p peak shifted toward a low binding energy. Two prominent peaks with binding energies of 780.85 and 796.72 eV correspond to Co^{3+} and the prominent peaks at 782.73 and 802.41 eV correspond to Co^{2+}. The high-resolution Ni 2p spectra indicate the existence of Ni^{2+}. It can be seen from the high-resolution spectrum of Fe 2p that the valence states of Fe ions are +3 and +2 (Figs. 3d and e). The high-resolution spectra of N 1s showed that the pyridine-N and pyrrole-N peaks in H3 were noticeably weak. The peaks at 406.6 and 402.81 eV can be attributed to nitrate and nitrate ions, which can be attributed to the charge balance between the layers of nitrate ions (Fig. S1a in Supporting information). In the O 1s high-resolution spectra, the peak positions of 531.22 and 532.11 eV can be attributed to O—C—O and C—OH, respectively (Fig. S1b in Supporting information). The peak positions of 284.67, 285.56 and 286.55 eV in the C 1s high-resolution spectrum can be attributed to C—C and C—O bonds (Fig. S1c in Supporting information).

The formation mechanism of the hollow structure was further studied. Iron nitrate, ammonium ferrous sulfate hexahydrate, and nickel nitrate hexahydrate were added to the ethanol dispersion of ZIF-67 to analyze the effects of different valence states of the same metal and different metals on the nanosheets and on the hollow structure. As can be seen in the TEM and SEM images (Fig. 4), the addition of Fe^{3+} and Fe^{2+} has no effect on the structure and morphology of ZIF-67, and no nanosheet or hollow structure has been formed. However, the introduction of Ni^{2+} results in the formation of surface nanosheets and internal hollow structures. The formation of the hollow and nanosheet structures can result from the hydrolysis of ions in the system, the different coordination ability of different ions with N, and the different number of nucleation sites. The hydrolysis acidity of Fe^{3+} is stronger than that of Ni^{2+} and Fe^{2+}. Further increasing the content of Fe^{3+} destroys the structure and eventually leads to the formation of a flaky structure (Fig. S2 in Supporting information). As shown in Fig. S3 (Supporting information), we analyzed the EDX-elemental mapping of increased $Fe(NO)_3{\cdot}6H_2O$ content in the lamellar structure. It can be seen that the destroyed structure still contains Fe, Co, Ni, C, N, O and other elements, but the carbon content is significantly reduced. To further study the effect of pH on the morphology, the change in pH of the solution in the reaction process was measured. It can be seen in Table S1 (Supporting information) that the addition of nickel ions significantly reduces the pH value, and the addition of Fe^{3+} further reduces it. After that, the pH remained nearly unchanged with time. The hydrolysis acidity of Fe^{2+} is weaker than that of Fe^{3+}, but the addition of Fe^{2+} results in a series of changes on the surface of ZIF-67, and etched traces appear on the surface, which may result from the stronger coordination ability of Fe^{2+} with N than that of Fe^{3+}. To further analyze the formation mechanism, we characterized and compared the color changes of the dispersion in the reaction process. As shown in Fig. S4

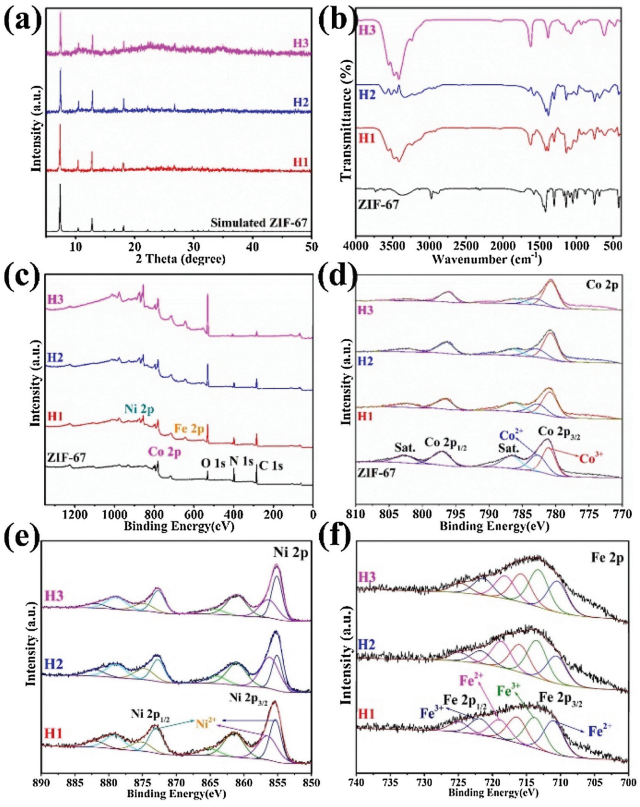

Fig. 3. (a) XRD of simulated ZIF-67, H1, H2 and H3. (b) FT-IR spectra of ZIF-67, H1, H2 and H3. (c) XPS full spectra of ZIF-67, H1, H2 and H3. (d) Co 2p spectra of ZIF-67, H1, H2 and H3. (e) Ni 2p spectra of H1, H2 and H3. (f) Fe 2p spectra of H1, H2 and H3.

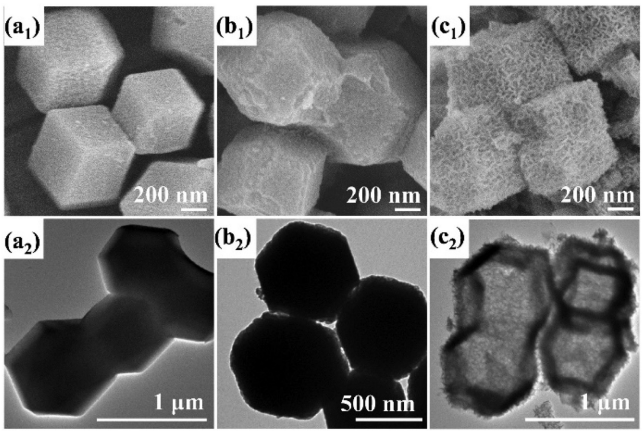

Fig. 4. SEM and TEM images of (a1, a2) only Fe(III) was added; (b1, b2) only Fe(II) was added; (c1, c2) only Ni(II) was added.

(Supporting information), the color of the ZIF-67 dispersion is purple; the addition of Ni^{2+} changes the color of the dispersion, and the addition of Fe^{3+} further changes the color of the solution. As the reaction proceeds, the purple color gradually fades, and the color of the dispersion gradually turns to yellow-green. The process of color change is consistent with that shown in Fig. 1a.

The capacitance performance of NiCoFeLDH@ZIF-67 in 3.0 mol/L KOH, was initially evaluated in a three-electrode system. The ZIF-67, H1, H2 and H3 electrodes were characterized by cyclic voltammetry (CV) at different sweep speeds with a voltage window of 0.48 V. All CV curves show a pair of noticeable redox peaks. This is due to the reversible Faraday reaction between the samples and the electrolyte OH^- ions, which indicates that all samples have good pseudo-capacitance characteristics. Sample H3 has a larger CV integration area and stronger redox peak than the other samples, indicating that the hollow structure material exhibits better pseudo-capacitance performance, larger specific capacity, and better charge storage performance. A pair of redox peaks appeared on the CV with the fixed potential window at different scan rates of 5–100 mV/s, indicating that the behavior of the capacitance was mainly controlled by the reversible Faraday redox reaction. With an increase in the scanning rate from 5 mV/s to 100 mV/s, the anode and cathode peaks shifted slightly in the direction with more positive and negative potentials, respectively. The shift of the peak position is due to the polarization of the electrode, resulting from the increase in the scanning rate (Fig. S7 in Supporting information).

The galvanostatic charge–discharge (GCD) curve shown in Fig. S6 (Supporting information) indicates that the charge–discharge time of electrode H3 is the longest. The specific capacitance values of ZIF-67, H1, H2 and H3 were 156.57, 337.19, 765.63 and 1202.08 F/g at 0.5 A/g, respectively. H3 had a larger specific capacitance compared with those of ZIF-67, H1 and H2, which is consistent with the CV results. In addition, compared with other MOF-related compounds, the hollow structure NiCoFeLDH@-ZIF-67 also had a higher specific capacitance (Table S2 in Supporting information). These results, combined with the analysis of the characterization results, suggest that the hollow structure material provides a suitable space for the deintercalation of ions and for the electrochemical reaction during the energy storage process. At current densities of 0.5, 1, 2, 3, 5, 10 and 20, the specific capacitances of H3 were 1202.08, 1200, 1172.5, 1160, 1114.58, 1045.83 and 947.08 F/g, respectively (Fig. S5d in Supporting information), exhibiting an excellent rate capability (78.79% from 0.5 A/g to 20 A/g). The specific capacity of the hollow structure is noticeably better than that of other structures. Fig. S5 (Supporting information) shows the GCD cycle of the ZIF-67, H1, H2 and H3 electrodes at different current densities (0.5–20 mA/cm^2) in the 0–0.48 V potential range. The GCD curve exhibits a plateau area of noticeable battery properties and shows good *pseudo*-capacitance characteristics.

NiCoFeLDH@ZIF-67 and activated carbon (AC) water-containing devices were used to further study the practical application of the NiCoFeLDH@ZIF-67 electrode in 3.0 mol/L KOH. Fig. S9 (Supporting Information) shows the CV curves of samples ZIF-67, H1, H2 and H3 at different scanning rates (10–100 mV/s). The CV curve maintains an appropriate shape at 100 mV/s, which indicates that the water-phase device has an excellent rate performance. In addition, all samples exhibit a pseudo-capacitance behavior.

The GCD curve of NiCoFeLDH@ZIF-67//AC (aqueous solution device) at 1 A/g is shown in Fig. S8 (Supporting information). The specific capacities of samples ZIF-67, H1, H2 and H3 were 32.31, 45.3, 71.83 and 112 F/g, respectively. Sample H3 had a larger specific capacity compared with those of ZIF-67, H1, and H2. The GCD curves of all samples exhibit a typical triangular symmetry and approximate linear distribution. The calculated specific capacitances of the H3//AC (aqueous solution devices) were 222.67, 164.93, 143.8, 133.33, 122.4 and 109.07 F/g, respectively, which were significantly higher than those of ZIF-67, H1 and H2 (Fig. 5). In addition, the capacitance retention rate of H3 after 1000 cycles was 62.1% (Fig. S10 in Supporting information). After 5000 cycles of testing, the XRD pattern indicates that the crystallinity of the material underwent a series of changes, indicating that the crystal structure of the material changed after a long cycling period (Fig. S11 in Supporting information). The chemical stability of ZIF-67 and NiCoFeLDH@ZIF-67 composite were characterized at 3 mol/L KOH. The original morphology of the hollow-structure NiCoFeLDH@ZIF-67 composite can be maintained after soaking in 3.0 mol/L KOH for 0 h, 12 h and 24 h. However, ZIF-67 appeared surface etching and flake clusters after 12 h, and the structure of ZIF -67 collapsed seriously after 24 h. The reason is that the structure of ZIF-67 is unstable under acidic and alkaline conditions. The transition metal hydroxyl compounds on the surface of the ZIF-67 can significantly improve the chemical stability of ZIF-67 structure in alkaline solution (Fig. S12 in Supporting information). To study the overall performance of H3//AC (aqueous system device), the relationship between the specific energy and specific power was determined according to the GCD curve of its two-electrode system (Fig. S13 in supporting information). The H3//AC showed a high specific energy of 69.58 Wh/kg at a specific power of 750.00 W/kg and 38.25 Wh/kg at 7500 W/kg, which were significantly higher than those of the other four devices. To verify the practical application of the hollow structure H3, two super-capacitors were charged in series to light up a blue light-emitting diode (LED).

In conclusion, we synthesized a hollow-structure NiCoFeLDH@-ZIF-67 composite and analyzed the structure formation mechanism. Without changing the basic structure of ZIF-67, we prepared conductive porous hollow nanomaterials, which could effectively improve the Faraday redox reaction. In a 3.0 mol/L KOH solution, the specific capacitance of the composite hollow structure was 1202.08 F/g at 1 A/g. Compared with ZIF-67 and other structural materials, this device had a higher specific capacitance when applied to supercapacitors. Studying the effect of different metal ions and different valence states of the same ion on the formation of hollow structures provides an effective method for the controllable synthesis of mesoporous materials. This study has a

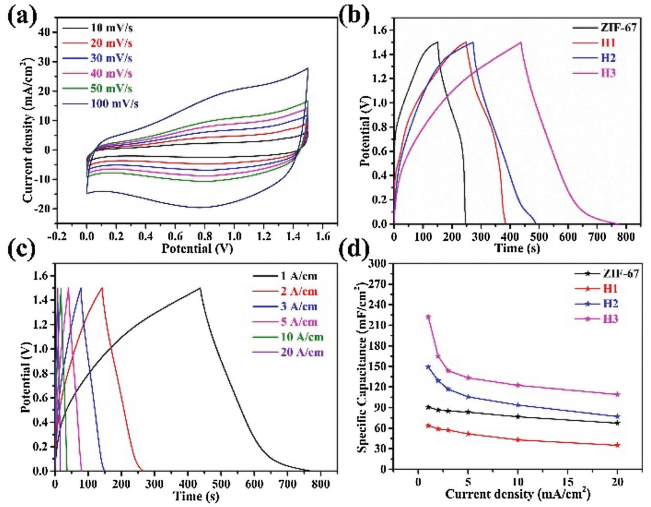

Fig. 5. Electrochemical properties of samples ZIF-67, H1, H2 and H3 in a two-electrode cell. (a) CV curves of H3 at different scanning speeds. (b) GCD curves of samples ZIF-67, H1, H2 and H3 at 1 A/g. (c) GCD curve of H3 at 1, 2, 3, 5, 10 and 20 A/cm^2. (d) The specific capacitance of ZIF-67, H1, H2 and H3 samples at different current densities.

certain guiding significance for the structure control of future MOFs.

Declaration of competing interest

The authors report no declarations of interest.

Acknowledgments

This work was supported by the National Natural Science Foundation of China (No. U1904215), Natural Science Foundation of Jiangsu Province (No. BK20200044), Changjiang scholars program of the Ministry of Education (No. Q2018270).

Appendix A. Supplementary data

Supplementary material related to this article can be found, in the online version, at doi:https://doi.org/10.1016/j.cclet.2021.03.050.

References

[1] Y. Hua, X. Li, C. Chen, H. Pang, Chem. Eng. J. 370 (2019) 37–59.
[2] J. Wang, N. Li, Y. Xu, H. Pang, Chem. Eur. J. 26 (2020) 6402–6422.
[3] X. Li, D. Ma, C. Cao, et al., Small 15 (2019) 1902218.
[4] B. Zhu, D. Xia, R. Zou, Coord. Chem. Rev. 376 (2018) 430–448.
[5] Q. Zhu, W. Xia, T. Akita, R. Zou, Q. Xu, Adv. Mater. 28 (2016) 6391.
[6] X. Meng, X. Xiao, H. Pang, Front. Chem. 8 (2020) 330.
[7] X. Xiao, G. Zhang, Y. Xu, et al., J. Mater. Chem. A 7 (2019) 17266–17271.
[8] C. Gu, J. Li, G. Yang, et al., Chin. Chem. Lett. 31 (2020) 2263 –226.
[9] Z. Liang, R. Zhao, T. Qiu, R. Zou, Q. Xu, EnergyChem 1 (2019) 100001.
[10] Y. Li, Y. Shan, H. Pang, Chin. Chem. Lett. 31 (2020) 2280–2286.
[11] H. Zhou, M. Zheng, H. Tang, et al., Small 16 (2019) 1904252.
[12] Z. Liang, C. Qu, W. Guo, R. Zou, Q. Xu, Adv. Mater. 30 (2017) 1702891.
[13] B. Zhu, R. Zou, Q. Xu, Adv. Energy Mater. 8 (2018) 1801193.
[14] H. Li, L. Li, R. Lin, et al., EnergyChem 1 (2019) 100006.
[15] L. Jin, H. Pang, Chin. Chem. Lett. 31 (2020) 2300–2304.
[16] S. Zheng, Y. Zheng, H. Xue, H. Pang, Chem. Eng. J. 395 (2020) 125166.
[17] X. Li, X. Yang, H. Xue, H. Pang, Q. Xu, EnergyChem 2 (2020) 100027.
[18] Y. Li, Y. Xu, Y. Liu, H. Pang, Small 15 (2019) 1902463.
[19] D. Zhou, X. Zhang, Z. Mo, et al., EnergyChem 1 (2019) 100016.
[20] W. Xia, C. Qu, Z. Liang, et al., Nano Lett. 17 (2017) 2788–2795.
[21] C. Qu, B. Zhao, Y. Jiao, et al., ACS Energy Lett. 2 (2017) 1263–1269.
[22] B. Liu, H. Shioyama, H. Jiang, X. Zhang, Q. Xu, Carbon 48 (2009) 456–463.
[23] C. Qu, Z. Liang, Y. Jiao, et al., Small 14 (2018) 1800285.
[24] Y. Wang, L. Yan, K. Dastafkan, et al., Adv. Mater. (2021) 2006351.
[25] Y. Ru, S. Zheng, H. Xue, H. Pang, Chem. Eng. J. 382 (2020) 122853.
[26] H. Tabassum, W. Guo, W. Meng, et al., Adv. Energy Mater. 7 (2017) 1601671.
[27] A. Mahmood, W. Guo, H. Tabassum, R. Zou, Adv. Energy Mater. 6 (2016) 1600423.
[28] Z. Xia, Q. Huang, S. Guo, FlatChem 17 (2019) 100129.
[29] B. Qiu, C. Yang, W. Guo, et al., J. Mater. Chem. A 5 (2017) 8081–8086.
[30] J. Yang, F. Zhang, H. Lu, et al., Angew. Chem. 127 (2015) 11039–11043.
[31] M. Du, Q. Li, Y. Zhao, C. Liu, H. Pang, Coord. Chem. Rev. 416 (2020) 213341.
[32] Z. Liang, C. Qu, D. Xia, R. Zou, Q. Xu, Angew. Chem. 57 (2018) 9604–9633.
[33] W. Guo, W. Xia, K. Cai, et al., Small 13 (2017) 1702049.
[34] H. Zhou, X. Li, Y. Li, M. Zheng, H. Pang, Nano-Micro Lett. 11 (2019) 40.
[35] C. Wang, X. Li, Q. Li, H. Pang, FlatChem 16 (2019) 100107.
[36] B. Li, H. Xue, H. Pang, Q. Xu, Sci. China Chem. 63 (2020) 475–482.
[37] Y. Shan, Y. Li, H. Pang, Adv. Funct. Mater. 30 (2020) 2001298.
[38] S. Gao, B. Fan, R. Feng, et al., Nano Energy 40 (2017) 462–470.
[39] D. Li, H.Q. Xu, L. Jiao, H. Jiang, EnergyChem 1 (2019) 100005.
[40] Y. Zheng, S. Zheng, H. Xue, H. Pang, J. Mater. Chem. A 7 (2019) 3469–3491.
[41] Y. Wang, Y. Wang, L. Zhang, C. Liu, H. Pang, Inorg. Chem. Front. 6 (2019) 2514–2520.
[42] R. Zhao, Z. Liang, R. Zou, Q. Xu, Joule 2 (2018) 2235–2259.
[43] P. Geng, S. Cao, X. Guo, et al., J. Mater. Chem. A 7 (2019) 19465–19470.
[44] X. Xuan, M. Qian, L. Han, et al., Electrochim. Acta 321 (2019) 134710.
[45] Z. Jiang, Z. Li, Z. Qin, et al., Nanoscale 5 (2013) 11770–11775.
[46] C. Xu, X. Kong, S. Zhou, et al., J. Mater. Chem. A 6 (2018) 24050–24057.